Spontaneous oscillations, beating patterns, and hydrodynamics of active microfilaments

Brato Chakrabarti and David Saintillan

Department of Mechanical and Aerospace Engineering, University of California San Diego,
9500 Gilman Drive, La Jolla, California 92093, USA

Cilia and flagella are ubiquitous in nature and are known to help in transport and swimming at the cellular scale by performing oscillations. Fundamental to these periodic waveforms is the core internal structure of the filaments known as the axoneme, consisting of an array of microtubule doublets, protein linkers, and dynein motors. In the presence of ATP, the collective action of the molecular motors drives internal sliding motions that are converted to spontaneous oscillations by a mechanism that still remains elusive. A sliding controlled axonemal feedback mechanism has recently been proposed and explored in the limit of small deformations, where it was shown to result in nonlinear amplitude selection through a mechanical regulation of dynein kinetics. Here, we build on that model to derive a more complete set of planar nonlinear governing equations that retains all the geometric nonlinearities, incorporates intrinsic biochemical noise and accounts for long-range, nonlocal hydrodynamic interactions. For a clamped filament, motor activity drives a Hopf bifurcation leading to traveling wave solutions that propagate from tip to base, in agreement with previous weakly nonlinear studies. Quite remarkably, our results demonstrate the existence of a second transition far from equilibrium, where nonlinearities cause a reversal in the direction of wave propagation and produce a variety of waveforms that resemble the beating patterns of swimming spermatozoa. We further extend the model to account for asymmetric ciliary beats and also allow for generalized dynein regulation mechanisms that can qualitatively reproduce *Chlamydomonas reinhardtii* flagellar dynamics. In the spirit of dimensional reduction, limit cycle representations are obtained for various waveforms and highlight the role of biochemical noise. We also analyze the velocity fields generated by the filaments and apply principal component analysis to derive low-order flow representations in terms of fundamental Stokes singularities that could be of use for constructing minimal models of swimming microorganisms.

I. INTRODUCTION

Cilia and flagella are thin hairlike cellular projections that play a variety of crucial roles where motion at the cellular level is required. Flagella, found on sperm cells and in a number of protozoa, enable swimming in viscous media by propagating bending waves along their axis [1]. Cilia are typically shorter than flagella and beat in an asymmetric whipping pattern. The coordinated beating in carpets of cilia gives rise to "metachronal waves" that allow organisms such as *Paramecium* to swim efficiently. Motile cilia also play a crucial role in ovum transport and in transport of mucus across the respiratory track, known as mucociliary clearance [2].

The movement of the cilium is produced by the bending of its core known as the axoneme. The axoneme architecture, which is illustrated in Fig. 1, has been remarkably conserved across evolution [4]. It involves nine peripheral microtubule doublets known as the "A–B" microtubules [1], which are arranged in regular intervals and centered around a pair of singlet microtubules. The
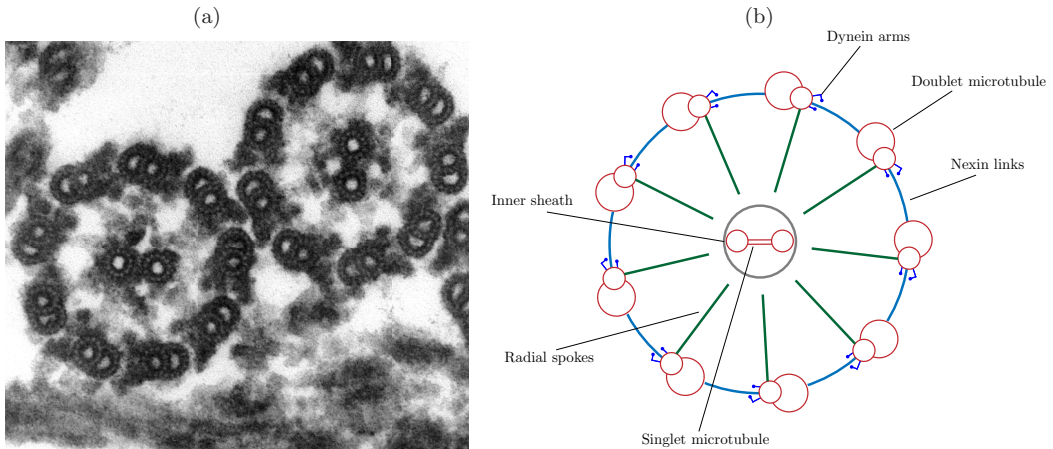
(a)

(b)

FIG. 1. (a) Thin section electron micrograph of axonemes of the green algae *Chlamydomonas reinhardtii*. Reproduced from Smith and Lefebvre [3]. (b) A simplified schematic of the cross-section of an axoneme showing the "9+2" structure.

outer doublets are linked to a sheath around the central pair by radial spokes and are connected among themselves through protein linkers known as nexin links. The network of links along with the radial spokes provide constraints that help to maintain the structural integrity of the axoneme. This characteristic arrangement of microtubules that extends for the entire length of the axoneme (10–$200\,\mu$m) is found in most eukaryotic flagella and cilia and is known as the "9+2" structure [1]. Thousands of dynein molecular motors are distributed along the A-tubule in groups that are responsible for force generation. The heads of these motors extend to the B-tubule of the adjacent doublet [5,6]. In the presence of adenosine triphosphate (ATP), the motor proteins undergo cycles of attachment and detachment generating forces that cause sliding between the doublets. It has been shown that in demembraneted flagellar axonemes this sliding can actually cause microtubules to slide apart [7]. However, inside cilia and flagella the protein linkers (nexin links) as well as the basal structure prevent free sliding, leading instead to bending deformations [1]. In swimming spermatozoa, these deformations take the form of bending waves that propagate along the flagellum from head to tip [6]. These highly coordinated motions suggest a complex regulation mechanism for the action of molecular motors along the length of the axoneme. While the structure of the axoneme and the mechanism for internal shear generation by dynein motors is understood [8], it still remains unknown how spontaneous oscillations can emerge from the coordinated action of thousands of molecular motors.

A number of approaches have been proposed to explain the spontaneous generation of oscillations in actuated elastic filaments. Several such models coarse-grain the role of molecular motors and the internal mechanics of the axoneme and focus instead on qualitative beating patterns that resemble those of cilia or flagella. One such recent approach [9–11] models the spontaneous oscillations observed in flagella as a buckling instability reminiscent of the classical flutter problem [12] in the presence of a follower-force. In a similar spirit, it was previously shown [13] that self-propelled Brownian particles connected as a chain can display periodic deformations that mimic ciliary beating patterns. In another model, Goldstein *et al.* [14] prescribed a suitable form of the internal shear force density to induce spontaneous oscillations resembling the bending waves seen in sperm.

However, there have also been considerable efforts over the last few decades in the development of theoretical models that capture some aspects of the geometric details of the axoneme and motor activity in an attempt to explain experimentally observed beating patterns. The bulk of

these models rely on some form of geometric feedback from the axoneme on the activity of the molecular motors. The three geometric features that may be involved in this feedback are: (a) curvature, (b) interdoublet distance, and (c) sliding displacement. In the curvature-controlled models, the dynein activity is regulated by the instantaneous curvature or by a delayed curvature of the axoneme [15–17]. Once the curvature exceeds a predefined threshold the dyneins are deactivated. This feedback mechanism was able to produce propagating wave patterns as observed in flagella [16,17] as well as ciliary beating patterns [15]. Recently it has been proposed [18] that the breaststrokelike beating patterns of *Chlamydomonas* are best explained through curvature-controlled feedback. However, these models coarse-grain the detailed kinetics of dynein activity. The geometric-clutch model [19] instead argues that dynein activity is regulated by interdoublet separation. This separation is governed by the transverse force generated from stretched nexin links in a bent configuration that further dictates the probability of formation of dynein bridges. The attachment and detachment of dynein is determined dynamically from the instantaneous transverse force. This model has been able to reproduce both flagellar and ciliary waveforms. While the initial discrete model [19] had a poor model of hydrodynamics, a recent continuum extension [20] includes a more detailed hydrodynamic model. It was shown by Ref. [20] that the excitable dynein model can be mapped back to the Fisher-Kolmorogov equation, which admits traveling wave solutions. However, as pointed out in Ref. [5], their model [21] does not lead to self-regulated saturation of the unstable modes of oscillation and instead relies on the addition of stiff non-linear springs. Finally, the sliding control model assumes a linear relationship between the internal shear force and sliding displacements. Other studies [22–24] have prescribed the internal shear force to have a form of traveling wave that results in spermlike beating patterns. However, this approach not only sets the intrinsic beating frequency but also coarse-grains the dynamics of the molecular motors. Sliding control models can also be equipped with a two-state model for molecular motors that depends on both the sliding displacement and the rate of sliding [6,25]. Beyond a critical activity of the motors, a Hopf bifurcation takes place leading to spontaneous oscillations of the filament. Numerical simulations [5,6,26] involving two-state models have been performed only close to the bifurcation threshold and in the small curvature limit. These simulations suggest that for a clamped filament bundle, bending waves propagate from the tip to the base (retrograde) as opposed to the base-to-tip (anterograde) propagation observed in swimming sperm. A change of boundary conditions [24] or including basal compliance [6] can affect the direction of bend propagation. Nevertheless, results from weakly nonlinear theories, while valid close to the bifurcation, may not provide an accurate picture of the far-from-equilibrium, geometrically nonlinear cases of beating.

Oriola *et al.* [5] recently proposed a detailed microscopic description of dynein kinetics coupled to flagellar shape in the framework of sliding controlled beating. Their model led to the saturation of unstable modes from nonlinear interactions without any additional need for nonlinear springs [20,21]. However, their analysis [5] was limited to the geometrically linear small-curvature limit close to the bifurcation. While the observed waves resembled flagellar waveforms, their direction was retrograde. In the present paper, we use the microscopic kinetic model of Oriola *et al.* [5] to derive a more complete set of nonlinear governing equations that include hydrodynamic interactions and can be solved numerically. We discover that, when all the nonlinearities are retained, anterograde bend propagation can occur away from the bifurcation and results purely from nonlinear interactions of the dynein activity with axoneme geometry and hydrodynamics.

The paper is organized as follows. First, we present in Sec. II the geometrically nonlinear model for a microtubule bundle and dynein activity that follows Oriola *et al.* [5]. We then discuss in Sec. III the various beating patterns away from equilibrium, transitions in the direction of wave propagation, and the dependence of the amplitude and frequency of the bending waves on the level of activity of molecular motors. The model is also modified to allow for the possibility of asymmetric beats, and we show that an appropriate choice of parameters can induce ciliary beating patterns. Following past studies [5,27], we analyze the beating patterns using principal component analysis in Sec. IV B. Finally, the disturbance velocity fields and their minimal representations in terms of fundamental singularities of Stokes flow both in free space and next to a no-slip wall are discussed in
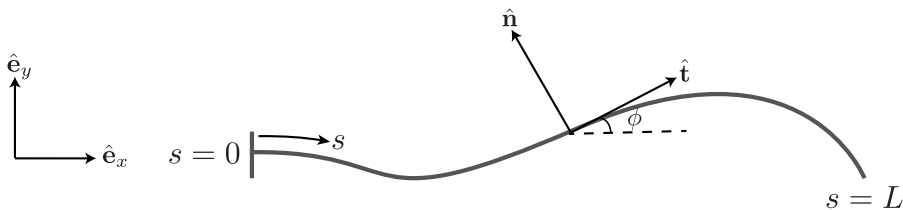
FIG. 2. Schematic of an elastic rod of length L and arclength s that is clamped at $s = 0$. The rod is represented as a space curve in the (x, y) plane, which we parametrize by the tangent angle $\phi(s, t)$.

Sec. V. These representations could provide a basis for studying hydrodynamic interactions between spontaneously beating filaments and potential mechanisms for synchronization. We summarize and conclude in Sec. VI.

II. MODEL FOR AXONEMAL BEATING

A. Viscous dynamics of an elastic filament

1. Geometry and force balance

We idealize a beating flagellum or cilium as an inextensible unshearable planar elastic rod submerged in a fluid with viscosity ν. Its motion is described by a set of geometrically nonlinear equations following Euler's elastica theory [28], with viscous stresses captured by nonlocal slender-body hydrodynamics as we explain in Sec. II A 2. As shown in Fig. 2, we consider a filament with length L and diameter a such that $\epsilon = a/L \ll 1$, where ϵ is the slenderness ratio. We impose that one end of the filament is fixed, as in the case of a cilium attached to a wall or a flagellum affixed to a sperm head, and we assume clamped boundary conditions at that end. We parametrize the filament centerline with arc-length $s \in [0, L]$, and in the case of planar deformations conformations are fully described by the tangent angle $\phi(s, t)$. Expressions for the tangent and normal vectors to the curve follow as

$$\hat{\mathbf{t}} = \cos\phi\,\hat{\mathbf{e}}_x + \sin\phi\,\hat{\mathbf{e}}_y, \tag{1}$$

$$\hat{\mathbf{n}} = -\sin\phi\,\hat{\mathbf{e}}_x + \cos\phi\,\hat{\mathbf{e}}_y. \tag{2}$$

Any point along the filament can be described alternatively by a Lagrangian marker $\mathbf{x}(s, t)$, which is given by

$$\mathbf{x}(s, t) = \mathbf{x}(0, t) + \int_0^s \hat{\mathbf{t}}(s', t)\,ds'. \tag{3}$$

Inextensibility of the filament results in a metric constraint on this Lagrangian marker: $\partial_s \mathbf{x} \cdot \partial_s \mathbf{x} = 1$. The velocity at any point on the filament can be projected onto the tangent and normal, yielding $\mathbf{v} = v_t \hat{\mathbf{t}} + v_n \hat{\mathbf{n}} \equiv \partial_t \mathbf{x}$. It can be shown after manipulations that the velocity components are related as

$$\partial_s v_t = (\partial_s \phi)\, v_n, \tag{4}$$

$$\partial_s v_n = \partial_t \phi - (\partial_s \phi)\, v_t. \tag{5}$$

The elastica is subjected to general contact forces $\mathbf{F}(s, t) = \sigma\hat{\mathbf{t}} + N\hat{\mathbf{n}}$ as well as contact moments $\mathbf{M}(s, t) = M\hat{\mathbf{k}}$. These have both passive and active contributions resulting from elasticity and from

molecular motor forces, which we discuss in Sec. II B. In the absence of inertia, force and torque balances on an arbitrary section (s_1, s_2) of the filament at any given instant t are written

$$\int_{s_1}^{s_2} \mathbf{f}_{\text{vis}}(s)\, ds + \mathbf{F}(s)\big|_{s_1}^{s_2} = \mathbf{0}, \tag{6}$$

$$\int_{s_1}^{s_2} \mathbf{x} \times \mathbf{f}_{\text{vis}}(s)\, ds + (\mathbf{x} \times \mathbf{F}(s) + \mathbf{M}(s))\big|_{s_1}^{s_2} = \mathbf{0}, \tag{7}$$

where $\mathbf{f}_{\text{vis}}(s, t)$ is the viscous force density exerted by the fluid on the filament. On using the fundamental theorem of calculus, we arrive at the two equations of motion:

$$\mathbf{f}_{\text{vis}} + \partial_s \mathbf{F} = \mathbf{0}, \tag{8}$$

$$M_s + N = 0, \tag{9}$$

where the moment balance reduces to a scalar equation for planar deformations, and $\partial_s \mathbf{F} \equiv \mathbf{f}_e(s, t)$ is the internal force density resulting from elastic and active stresses.

2. Slender-body hydrodynamics

The typical Reynolds number for flagella or cilia can be estimated to be $\mathcal{O}(10^{-4} - 10^{-5})$, and we thus assume Stokes flow. Given the assumption of slenderness $\epsilon \ll 1$, we model viscous stresses using nonlocal slender-body theory [29–32], which relates the Lagrangian velocity to the viscous force density $\mathbf{f}_{\text{vis}} = -\mathbf{f}_e$ through a linear relation of the form

$$8\pi \nu\, \mathbf{v} = -\mathcal{M}[\mathbf{f}_{\text{vis}}] = \mathcal{M}[\mathbf{f}_e], \tag{10}$$

where $\mathcal{M}$ is the configuration-dependent mobility operator that can be split into two parts: $\mathcal{M} = \mathcal{L} + \mathcal{K}$. The first term $\mathcal{L}$, known as the local operator, accounts for local drag anisotropy and is given by

$$\mathcal{L}[\mathbf{f}_e](s) = [(2 - c)\hat{\mathbf{n}}(s)\hat{\mathbf{n}}(s) - 2c\hat{\mathbf{t}}(s)\hat{\mathbf{t}}(s)] \cdot \mathbf{f}_e(s), \tag{11}$$

where $c = \log(\epsilon^2 e) < 0$ with $\epsilon = a/L$. By analogy with resistive force theory [33,34] and for later convenience, we also introduce local anisotropic friction coefficients

$$\xi_{\parallel} = -\frac{1}{2c}, \quad \xi_{\perp} = \frac{1}{2 - c}, \tag{12}$$

which satisfy the well-known property: $\xi_{\perp}/\xi_{\parallel} \to 2$ as $\epsilon \to 0$. The second term $\mathcal{K}$ in the mobility relation captures hydrodynamic interactions between distant parts of the filament. It is given by a nonlocal integral operator,

$$\mathcal{K}[\mathbf{f}_e](s) = \int_0^L \left[\frac{\mathbf{I} + \hat{\mathbf{R}}(s, s')\hat{\mathbf{R}}(s, s')}{|\mathbf{R}(s, s')|} \cdot \mathbf{f}_e(s') - \frac{\mathbf{I} + \hat{\mathbf{t}}(s)\hat{\mathbf{t}}(s)}{|s - s'|} \cdot \mathbf{f}_e(s) \right] ds', \tag{13}$$

where $\mathbf{R}(s, s') = \mathbf{x}(s) - \mathbf{x}(s')$ and $\hat{\mathbf{R}} = \mathbf{R}/|\mathbf{R}|$. For the sake of simplicity, we also introduce the notations

$$u_t^d(s) = \mathcal{K}[\mathbf{f}_e](s) \cdot \hat{\mathbf{t}}(s), \quad u_n^d(s) = \mathcal{K}[\mathbf{f}_e](s) \cdot \hat{\mathbf{n}}(s). \tag{14}$$

Using these definitions along with relations Eqs. (4) and (5), we can rewrite the equations of motion along the tangent and normal directions. After algebraic manipulations and using the fact that $\partial_s \hat{\mathbf{n}} =$

$-(\partial_s \phi)\,\hat{\mathbf{t}}$, we arrive at

$$\sigma_{ss} - \left(1 + \frac{\xi_\parallel}{\xi_\perp}\right)N_s\phi_s - N\phi_{ss} - \frac{\xi_\parallel}{\xi_\perp}\sigma\phi_s^2 = \xi_\parallel\left(\phi_s u_n^d - \partial_s u_t^d\right), \tag{15}$$

$$N_{ss} - \frac{\xi_\perp}{\xi_\parallel}N\phi_s^2 + \sigma\phi_{ss} + \left(1 + \frac{\xi_\perp}{\xi_\parallel}\right)\sigma_s\phi_s = \xi_\perp\left(8\pi\nu\,\phi_t - u_t^d\phi_s - \partial_s u_n^d\right), \tag{16}$$

$$M_s + N = 0, \tag{17}$$

which are statements of the tangential force, normal force and moment balances, respectively. Our primary focus in this paper is on filament dynamics in free space. However, we have also performed limited simulations of clamped filaments against a no-slip wall, for which we account for the disturbance velocity field $\mathbf{u}^d$ using Blake's Green's function [35].

3. Boundary conditions

We assume the filaments have one fixed end at $s = 0$, and thus $v_t(0, t) = v_n(0, t) = 0$. On using the force balance in the tangential and normal directions at $s = 0$, this condition results in

$$(\sigma_s - N\phi_s)|_{s=0} = 0, \quad (N_s + \sigma\phi_s)|_{s=0} = 0. \tag{18}$$

The other end of the filament at $s = L$ is force- and torque-free, which translates to

$$\sigma(L, t) = N(L, t) = M(L, t) = 0. \tag{19}$$

For a clamped filament that cannot rotate about the fixed point we prescribe a fixed orientation of the tangent vector. Without loss of generality, we will assume that $\hat{\mathbf{t}}(0, t) = \hat{\mathbf{e}}_x$, and therefore

$$\phi(0, t) = 0. \tag{20}$$

We have yet to specify the nature of the active internal forces and induced moments that drive the filament dynamics. Next, we present the model for internal axoneme mechanics and for the kinematics of molecular motors that are responsible for spontaneous oscillations.

B. Force and moment densities and motor kinetics

As a simplified model for the cross-linked flagellar bundle that composes the axoneme, we resort to a two-dimensional projection of the three-dimensional structure as illustrated in Fig. 3. In the complete "9+2" structure, the molecular motors connecting pairs of doublets lead to sliding forces that result in deformations. The structure of the axenomal cross-section, as depicted in Fig. 1, involves a cyclic arrangement of the dyneins, and therefore motors on opposite sides of the axoneme operate antagonistically, as in a "tug-of-war." To capture this process within a minimal framework, we follow previous models [5,6] and idealize the axoneme as a pair of two polar elastic filaments $(+)$ and $(-)$ separated by a constant distance a that are able to deform in tandem in the plane of motion. The centerline of this projected bundle is described by $\mathbf{x}(s, t)$ and the positions of the two filaments are given by $\mathbf{x}_\pm(s, t) = \mathbf{x}(s, t) \pm (a/2)\hat{\mathbf{n}}(s, t)$, where $\hat{\mathbf{n}}$ is the unit normal along the centerline.

Dynein motors extend from each filament and bind with and walk along the opposite one, with the former acting as cargo. As the motors are activated, they push on both filaments and thereby exert tangential sliding forces $\pm f(s, t)$. These forces result in internal moments that can cause bending and induce an arc-length mismatch between the two filaments, known as the sliding displacement:

$$\Delta(s, t) = \int_0^s (|\partial_s \mathbf{x}_-| - |\partial_s \mathbf{x}_+|)ds' = a[\phi(s, t) - \phi_0], \tag{21}$$

where $\phi_0 = \phi(0, t) = 0$ for clamped boundary conditions. The relative sliding of the two filaments is not free, as it is resisted by nexin protein cross-linkers that act as linear springs and also contribute to the net internal shear force. Indeed, as mentioned previously, microtubules can actually slide apart
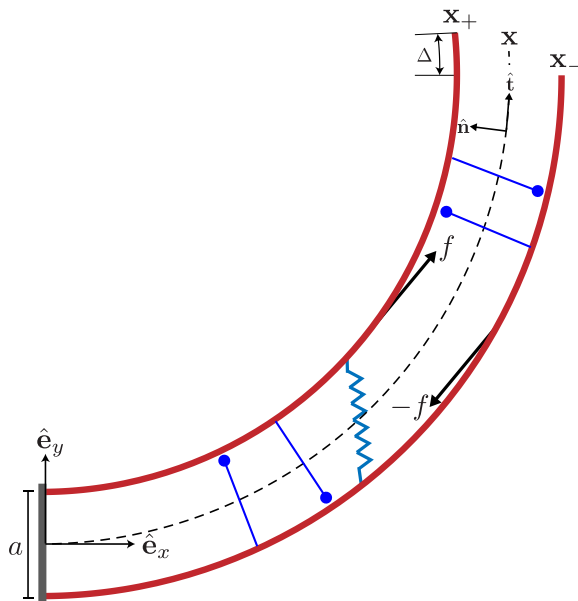
FIG. 3. Schematic of the simplified two-dimensional projection of the axoneme. In this model, the axoneme is composed of two polar filaments $\mathbf{x}_+$ and $\mathbf{x}_-$ and has centerline $\mathbf{x}$. Nexin links are shown as elastic springs that resist sliding Δ. Mechanical loads exerted by bound dynein motors result in an internal shear force density $\pm f(s, t)$ that acts in the opposite direction on the two filaments, generating an active internal moment.

in the absence of these linkers in demembraneted flagellar axonemes [7]. Following Oriola *et al.* [5], we model the sliding force density by coarse-graining the activity of the motors as

$$f(s, t) = \rho(n_+ F_+ + n_- F_-) - K\Delta. \tag{22}$$

Here, $\rho = \mathcal{N}/L$ is the mean density of motors along both filaments, and $n_\pm$ are the fractions of motors on the $(+)$ and $(-)$ filaments that are in the bound state. $F_\pm$ is the load exerted by individual $(+)$ and $(-)$ motors and K is the effective spring stiffness of the nexin cross-linkers.

By the law of action and reaction, the sliding forces $\pm f(s, t)$ are equal and opposite on both filaments, and thus the net active force on an axonemal cross-section is zero. However, an active internal moment is generated and competes against bending elasticity, yielding

$$M(s, t) = B\phi_s - aF, \tag{23}$$

where B is the net bending rigidity of the filament bundle and $F(s, t) = \int_s^L f(s', t)ds'$. The first term is the passive response from Euler-Bernoulli beam theory, while the second term captures the action of molecular motors. On inserting this expression in the moment balance Eq. (17), we obtain

$$B\phi_{ss} + af(s, t) + N = 0, \tag{24}$$

where N is the contact force in the normal direction. This relation highlights the mechanism by which the internal force density generated from bound dynein motors induces internal moments that can cause bending and deformations of the bundle.

To complete the description of internal active forces, we must model motor binding kinetics as well as motor loads. The dynein kinetics is described by a two-state mechanochemical model consisting of bound and unbound dyneins, with a constant total number $\mathcal{N}$ of dyneins (bound or unbound) on both filaments. A single motor can bind with the opposite filament with rate π and

unbind with rate ϵ. The evolution of the bound motor populations is described as

$$\partial_t n_\pm = \pi_\pm - \epsilon_\pm. \tag{25}$$

The binding rate is proportional to the local fraction of unbound motors and given by $\pi_\pm = \pi_0(1 - n_\pm)$, where π_0 is the characteristic rate constant. The unbinding rate of molecular motors is known to depend on the carried load [36]. In particular, experiments with kinesin motors have shown that the dissociation rate increases exponentially with F, and this functional dependence has previously been used in models of bidirectional cargo transport by molecular motors [37] and of dynein kinetics inside the axoneme [6]. Consistent with previous studies [5,6], we thus express the detachment rate as $\epsilon_\pm = \epsilon_0 n_\pm \exp(F_\pm/f_c)$, where f_c is a critical load beyond which rapid detachment takes place. We would like to emphasize, however, that the emergent filament dynamics explored in the following sections is insensitive to this functional choice, provided that the detachment rate increases sufficiently fast with the carried load. Following previous models [5,37] and experiments [36], we also assume a linear force–velocity relationship for the molecular motors. At stall force f_0, the motors are at complete rest, and the zero load velocity is v_0. Intermediate loads can then be estimated by linear interpolation as $F_\pm = \pm f_0(1 \mp \Delta_t/v_0)$, where $\Delta_t = a\phi_t$ is the sliding velocity. With these assumptions, the internal sliding force density of Eq. (22) becomes

$$f(s,t) = f_0\rho\left(\bar{n} - \frac{\Delta_t}{v_0}\tilde{n}\right) - K\Delta, \tag{26}$$

where $\bar{n} = n_+ + n_-$ and $\tilde{n} = n_+ - n_-$. It is well known that the binding and unbinding of motors is a stochastic process due to the presence of intrinsic biochemical noise. In order to model this effect, we also incorporate a multiplicative noise term in Eq. (25) of the form $n^{br}(s,t) = T_{\text{eff}}\delta(t - t')\delta(s - s')$, where T_{eff} is an effective temperature and where the noise is delta-correlated in both space and time. Including fluctuations and the expressions for the binding and unbinding rates, we rewrite the evolution equation for the fractions of bound motors as

$$\partial_t n_\pm = \pi_0(1 - n_\pm) - \epsilon_0 n_\pm \exp\left[\frac{f_0}{f_c}(1 \mp \Delta_t/v_0)\right] + n^{br}(s,t). \tag{27}$$

This completes the model for motor kinetics and internal forces. It is important to emphasize the two-way feedback that exists between filament geometry and dynamics and the kinetics of bound motors. Dynein activity causes internal shear and sliding of the filaments, which contributes to the active moment. In turn, the sliding displacement causes load-dependent binding and unbinding of motors and affects the magnitude of the internal shear force, possibly giving rise to filament oscillations.

C. Nondimensionalization

We nondimensionalize arc-length by L and time by the characteristic correlation time $\tau_0 = 1/(\epsilon_0 + \pi_0)$ of the dynein motors. The scale for internal elastic forces is given by the characteristic bending force B/L^2, which implies $\mathcal{M}[\mathbf{f}_e] \sim B/L^3$, and finally the internal motor force density is scaled by ρf_0. It is also evident from the expression of the sliding displacement that its appropriate scale is the axoneme diameter a. Nondimensionalization of the governing equations results in four dimensionless parameters: (a) $\text{Sp} = L(8\pi\nu/B\tau_0)^{1/4}$ is the sperm number that compares the characteristic time scale of relaxation of a bending mode to the motor correlation time. Smaller values of Sp describe short and rigid filaments. (b) $\mu = Ka^2L^2/B$ compares the elastic forces generated by the nexin links due to sliding to the characteristic magnitude of bending forces. (c) $\mu_a = a\rho f_0 L^2/B$ is the measure of motor activity (that is proportional to the active force) compared to bending forces. (d) $\zeta = a/(v_0\tau_0)$ compares the diameter of the filament bundle to the characteristic displacement due to motor activity.

With these scales, the dimensionless force density reads $f(s,t) = \bar{n} - \zeta\,\tilde{n}\Delta_t - (\mu/\mu_a)\Delta$, and the nondimensionalized equations of motions are then given by

$$\sigma_{ss} - \left(1 + \frac{\xi_\parallel}{\xi_\perp}\right)N_s\phi_s - N\phi_{ss} - \frac{\xi_\parallel}{\xi_\perp}\sigma\phi_s^2 = \xi_\parallel\big(\phi_s u_n^d - \partial_s u_t^d\big), \tag{28}$$

$$N_{ss} - \frac{\xi_\perp}{\xi_\parallel}N\phi_s^2 + \sigma\phi_{ss} + \left(1 + \frac{\xi_\perp}{\xi_\parallel}\right)\sigma_s\phi_s = \xi_\perp\big(\mathrm{Sp}^4\,\phi_t - u_t^d\phi_s - \partial_s u_n^d\big), \tag{29}$$

$$\phi_{ss} + \mu_a f + N = 0. \tag{30}$$

The dimensionless stochastic equations for bound motor populations read

$$\partial_t n_\pm = \eta(1 - n_\pm) - (1 - \eta)n_\pm \exp[f^*(1 \mp \zeta\,\Delta_t)] + \Lambda w_\pm, \tag{31}$$

where $\eta = \pi_0/(\epsilon_0 + \pi_0)$ is the duty ratio, $f^* = f_0/f_c$ is the ratio of the stall force to the characteristic unbinding force, $w_\pm$ is a random vector drawn from a Gaussian distribution with zero mean and unit variance, and Λ is a numerical parameter characterizing the strength of biochemical noise. To solve the above equations numerically we use the expression for ϕ_t from Eq. (29) and insert it in the expression for the sliding velocity involved in the internal force density $f(s,t)$, which then enters the moment balance Eq. (30). On doing so, we obtain

$$\mu_a\zeta\,\tilde{n}\left[N_{ss} - \frac{\xi_\perp}{\xi_\parallel}N\phi_s^2 + \sigma\phi_{ss} + \left(1 + \frac{\xi_\perp}{\xi_\parallel}\right)\sigma_s\phi_s\right] - \xi_\perp\mathrm{Sp}^4 N$$
$$= \xi_\perp\mathrm{Sp}^4(\phi_{ss} + \mu_a\bar{n} - \mu\phi) - \xi_\perp\mu_a\zeta\,\tilde{n}\big(u_t^d\phi_s + \partial_s u_n^d\big). \tag{32}$$

The above system of equations is subject to boundary conditions Eqs. (18), (19), and (20).

D. Numerical methods and parameter selection

We solve the system of governing equations numerically by discretizing the filament arc-length into $M - 1$ equal segments of size $\Delta s = L/(M - 1)$. Spatial derivatives are handled using a second order accurate finite difference scheme. Nonlocal terms arising from hydrodynamic interactions result in a dense linear system for the unknown tension σ and normal force N; to avoid this costly system inversion, we instead employ an iterative method. For a given filament conformation, we first solve for σ and N using Eqs. (28) and (32) with the nonlocal terms evaluated at the previous time step. This problem results in a band-diagonal linear system of size $2M \times 2M$ that can be solved at a cost of $\mathcal{O}(2M)$. While doing so we use zero velocity at the base and zero force at the end of the filament as boundary conditions. We then evaluate the nonlocal terms and re-compute the tension and normal forces. This process is repeated until convergence, and typically three or four iterations are required. Once σ and N are known, we use Eq. (29) to march forward in time. This is done by a second order accurate backward-difference scheme along with the clamped boundary condition at $s = 0$ and the moment free condition at $s = L$. The evolution equation for the bound dynein motors given by Eq. (31) is marched forward independently using an implicit Euler–Maruyama scheme, which is adequate given the stochastic term. The numerical parameter Λ characterizing the strength of noise in Eq. (31) is related to the effective temperature T_{eff} as $\Lambda = (T_{\mathrm{eff}}/\Delta s\Delta t)^{1/2}$, where Δt is the simulation time step. Our numerical method scales linearly with the number of discretization points. In most results presented here, we use $M = 64 - 128$ and $\Delta t = 5 \times 10^{-4} - 1 \times 10^{-5}$.

The model involves a fairly large number of parameters, many of which can be estimated from direct experimental measurements based on sperm flagella and the green alga *Chlamydomonas reinhardtii*. In most calculations and unless otherwise noted, we use the parameter values provided by Bayly and Wilson [20] and Oriola *et al.* [5], which are summarized in Table I. Note that the motor correlation time τ_0, which sets the time scale in our model, is not known from measurements

TABLE I. Table listing the numerical values of the dimensional parameters as reported in various experiments.

Parameter	Numerical value	Description
a	200 nm	Effective diameter of the axoneme [6]
L	50 μm	Length of human sperm flagellum [38]
B	$0.9 - 1.7 \times 10^{-21}$ N m^2	Range of bending rigidity of sea-urchin sperm and bull sperm [6,20]
K	2×10^3 N m^{-2}	Interdoublet elastic resistance measured for *Chlamydomonas* [5]
$\xi_{\perp}$	$10^{-3} - 1$ Pa s	Range of coefficient of normal drag in different viscous media [5,20]
f_0	$1 - 5$ pN	Stall force for motor dynamics [5]
f_c	$0.5 - 2.5$ pN	Characteristic unbinding force of the motors [39]
v_0	$5 - 7$ μm/s	Motor walking speed at zero load [39]
τ_0	50 ms	Correlation time of motor activity [5]
ρ	10^3 μm^{-1}	Mean number density of motors [5]

and must be guessed; its chosen value results in a beating frequency of 10 Hz similar to a human spermatozoa [5]. Based on these values, we estimate the relevant dimensionless groups in Table II. The sperm number Sp and activity number μ_a are found to have the widest ranges, allowing for various dynamical transitions and beating patterns as we explore next.

III. SPONTANEOUS FILAMENT OSCILLATIONS

In this section, we systematically explore the parameter space through numerical simulations of the nonlinear equations and characterize transitions to spontaneous oscillations and beating patterns. A summary of the various dynamical regimes and beating patterns in the (Sp, μ_a) parameter space is presented as a phase chart in Fig. 4.

A. Linear stability and geometrically linear regime

Before analyzing dynamics far from equilibrium, we briefly review results of the linear stability analysis of Oriola *et al.* [5] and discuss the geometrically linear regime of small curvature. The stability analysis reveals that for a given sperm number Sp there exists a critical activity level μ_a^{crit} above which the filament undergoes a Hopf bifurcation. Above the bifurcation, a linear mode becomes unstable and grows exponentially while oscillating with a characteristic frequency ω. The critical activity was reported to increase almost linearly with sperm number [5] as also observed in our simulations in Fig. 4. Note that Oriola *et al.* [5] used local resistive force theory instead of nonlocal slender body hydrodynamics, and thus the instability threshold they predict differs quantitatively from the one we observe. Nonetheless, our method was found to reproduce their results if we neglect the nonlocal operator $\mathcal{K}$ and choose $\xi_{\perp}/\xi_{\parallel} = 2$ in the local mobility tensor. An increase in sperm number can be interpreted as an increase in viscosity resulting in larger viscous drag forces. As a result, a higher motor activity is required to induce an instability [40].

TABLE II. Range of the dimensionless groups of the problem estimated using the parameter values of Table I.

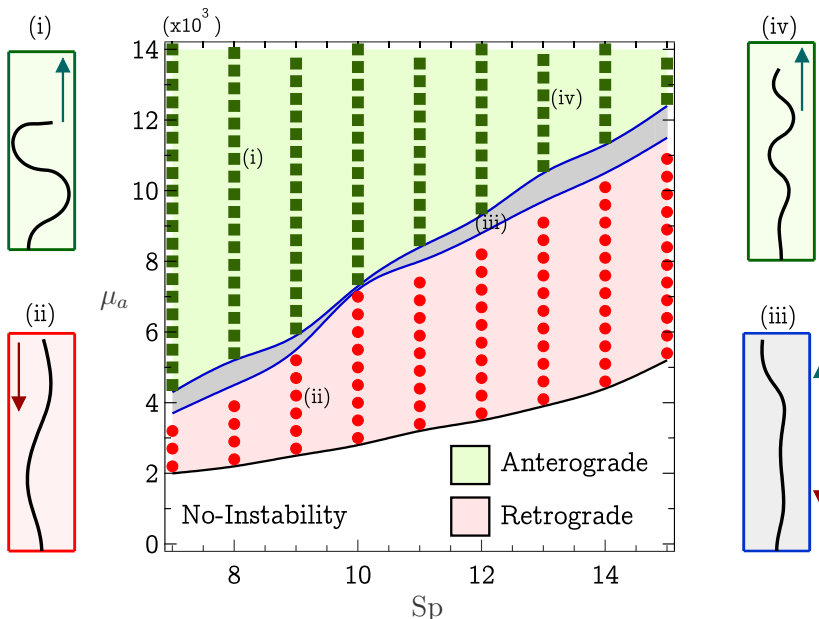| Dimensionless number	Numerical value
Sp $\equiv L(\xi_{\perp}/B\tau_0)^{1/4}$	5–20
$\mu_a \equiv af_0\rho L^2/B$	2–10 $\times 10^3$
$\mu \equiv Ka^2L^2/B$	50–100
$f^* \equiv f_0/f_c$	2
$\zeta \equiv a/v_0\tau_0$	$\mathcal{O}(1)$

FIG. 4. Phase chart highlighting the various dynamical transitions and beating patterns in the (Sp, μ_a) parameter space. Waveforms on both sides show characteristic filament conformations, where the arrows indicate the direction of wave propagation. Also see movie of the dynamics in the Supplemental Material [42]. Shown simulations are for $\mu = 100$, $\zeta = 0.3$, and $\eta = 0.14$.

One can also appreciate this result based on reduced-order models of molecular-motor-induced oscillations [25,41]. In these minimal models, the filament backbone is represented by a single lumped coordinate X and elasticity by a spring constant k with a viscous damping of strength ζ. Larger sperm number can then be interpreted as increased damping, resulting in an increased activity threshold for the onset of spontaneous oscillations.

Close to the bifurcation, the instability induces a traveling wave that propagates along the filament from tip to base (retrograde propagation). This direction of propagation is a common feature of linearized sliding control models with clamped boundary conditions [14,21,23,24] but is inconsistent with the well-known beating patterns of swimming spermatozoa, which exhibit anterograde wave propagation from base to tip. It is important to point out that, unlike curvature control models, the present formulation has no inherently preferred direction of wave propagation, which instead is selected spontaneously by linear and nonlinear feedback mechanisms [6,8]. Our results are consistent with linear predictions [5], which also show tip-to-base propagation near the Hopf bifurcation. Interestingly, most previous studies have focused on the geometrically linear or weak activity regimes and have overlooked nonlinear couplings. It is unclear *a priori* whether linear results adequately describe far-from-equilibrium dynamics, where the effects of nonzero tension and geometric nonlinearities become significant.

B. Large deformations in the nonlinear regime

Further away from the bifurcation, our numerical simulations of the fully nonlinear sliding-control model reveal a second transition to base-to-tip (anterograde) wave propagation. This transition occurs at approximately twice the critical level of activity required to trigger the first onset of oscillations: it is a truly nonlinear phenomenon that involves saturation of motor kinetics in the presence of large deformations and internal tension forces, and is beyond the scope of previously
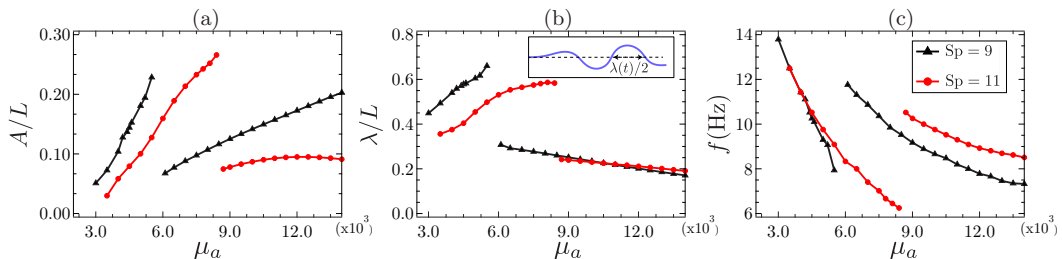
FIG. 5. Dependence of (a) dimensionless amplitude, (b) dimensionless wavelength, and (c) frequency of the beating patterns on motor activity μ_a for two values of the sperm number Sp. The dimensional frequency assumes the choice of $\tau_0 = 50$ ms for the motor correlation time. Jumps in the data are associated with the transition from retrograde to anterograde wave propagation. Simulations were performed with $\mu = 100$, $\zeta = 0.3$, and $\eta = 0.14$.

studied linearized [5] or weakly nonlinear [23] models. It is worth noting that Bayly and Wilson [21] did study nonlinear dynamics using a variant of the sliding-control model presented here. They were unable to observe anterograde propagation even at finite amplitudes, and we attribute this discrepancy to their model for the sliding force density, which did not involve feedback from nexin links, and to their specific choice of dynein kinetics, which did not allow for self-sustained saturation. The transition from retrograde to anterograde wave propagation with increasing motor activity occurs through a narrow transitional band of intermediate states (gray region in the phase chart of Fig. 4), whose width varies slightly with sperm number. The dynamics in this regime appears chaotic and combines standing waves with waves that switch quasiperiodically between the two directions of propagation (see Supplemental Material [42] for movies illustrating these features). We also note that the emergence of anterograde wave propagation is primarily due to the geometric nonlinearities and happens even in the absence of nonlocal hydrodynamic interactions.

In addition to changes in the direction of wave propagation, it is apparent from the characteristic waveforms shown in Fig. 4 that both sperm number and motor activity affect the qualitative features of the beating patterns. We explore these variations in Fig. 5, showing the dependence of amplitude, wavelength and frequency of the waveforms as a function of μ_a for two different values of Sp. For measuring wavelength, we determine the zero crossings of a given waveform, measure the distance between them as shown in the inset of Fig. 5(b), and average it over one period of motion to obtain λ. In the retrograde regime, the amplitude and wavelength both increase monotonically with activity, while the beating frequency decreases. The second transition to anterograde propagation causes all quantities to change abruptly as seen in Fig. 5. After a significant reduction across the transition, the amplitude starts to grow again with activity. Since the filament is inextensible, this increase in amplitude is accompanied by a slight decrease in wavelength. The frequency of oscillations increases with the transition to anterograde waves and then decreases monotonically with μ_a. Recall that all times in the model are scaled by the characteristic motor correlation time τ_0. We find that setting its value to $\tau_0 = 50$ ms produces dimensional beating frequencies in the range of $f \sim 6$–14 Hz.

At a fixed μ_a, increasing Sp tends to reduce the amplitude as viscous resistance becomes more important. It may seem counterintuitive that the wavelength of oscillations varies very little with Sp in the anterograde regime while the amplitudes differ significantly. This stems from the fact that, at low sperm numbers and high activity levels, the oscillations result in strong swaying motions as shown in Fig. 4(i) and movies in the Supplemental Material [42]. These large angular oscillations contribute to the large amplitudes observed in Fig. 5(a) for Sp = 9. A typical waveform resembling that of sperm cells is shown in Fig. 6(a) and was obtained for Sp = 12. In the simulation shown, waves propagate from base to tip with a frequency of $f \approx 8.8$ Hz, which is consistent with that of spermatozoa.
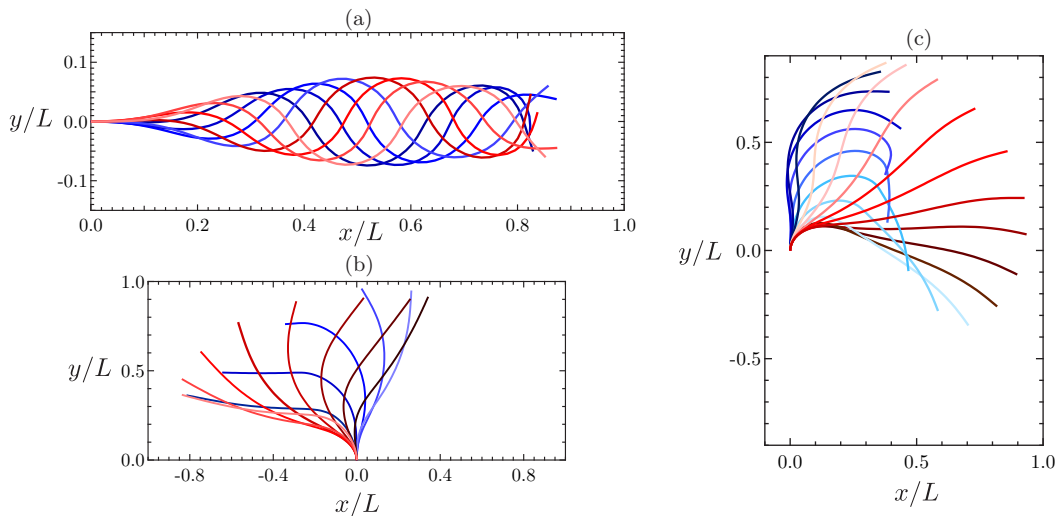
FIG. 6. Overlaid characteristic waveforms at different time instants over the course of one beating period: (a) Symmetric spermlike beat. Parameters: Sp $= 12$, $\mu_a = 12 \times 10^3$ and $\mu = 100$. (b) Asymmetric cilialike beat obtained with biased dynein kinetics. Parameters: Sp $= 2.5$, $\mu_a = 2 \times 10^3$, $\mu = 90$, $(\pi_0^+, \epsilon_0^+) = (0.17, 0.73)$, and $(\pi_0^-, \epsilon_0^-) = (0.25, 0.75)$. (c) Asymmetric beating pattern resembling *Chlamydomonas*, obtained with biased kinetics in presence of both sliding and curvature control. Parameters: Sp $= 2.2$, $\mu_a = 1.5 \times 10^3$, $\mu = 80$, $f^* = 1.9$, $(\pi_0^+, \epsilon_0^+) = (0.24, 0.76)$, $(\pi_0^-, \epsilon_0^-) = (0.39, 0.61)$, $\kappa^0 = -2.0$, and $\kappa_c = 12$. Also see movies in the Supplemental Material [42].

C. Asymmetric beating patterns

The same "9+2" microtubule doublet structure that is found in sperm flagella also appears in pair in the biflagellate alga *Chlamydomonas reinhardtii*, which swims in a breaststroke fashion. It is also present in the ciliary structures that cover epithelial cells as well as unicellular organisms such *Paramecium* where they beat in asymmetric whipping patterns. The asymmetric beating of cilia is key to metachronal coordination in ciliary carpets that are useful for micro-organism motility as well as pumping and transport of fluid in the body. We now discuss modifications of the sliding control model that allow it to produce asymmetric beating patterns qualitatively similar to those of cilia and *Chlamydomonas*.

1. Ciliary beating: Biased kinetics

The generation of asymmetric beat patterns in models for cilia has previously been approached in several ways. A geometric switch mechanism was proposed in Refs. [15,43] with a detailed model of internal nexin links exerting forces on the microtubules that produced spontaneous oscillations of the filament. Dynein activation was initiated based on local microtubule curvature, allowing for asymmetric beats with a typical frequency of $f \sim 50$–100 Hz. A two-state model of molecular motors [25] was used in Ref. [26] to generate spontaneous oscillations close to the bifurcation limit, where an external flow was used to break the symmetry of beating. Another set of models with an internal "engine" that coarse-grains dynein activity into a geometric-conformation-driven shear force was proposed in Refs. [44,45] to generate cilialike beating. Most recently, it was shown [46] that geometric constraints with a dynamical law for tension can also generate asymmetric ciliary beating patterns. Most of these approaches, however, have not included detailed motor kinetics. Here, we show that asymmetric beating patterns that resemble those of cilia can be obtained within our sliding-control model through a biased dynein kinetics. This is inspired by the recent

continuum formulation of Bayly and Wilson [20] of the geometric-clutch model [19], where a biased attachment-detachment probability was used to generate *Chlamydomonas*-like breaststrokes.

Biased kinetics is simply achieved by specifying distinct values for the characteristic binding and unbinding rate constants $\pi_0^{\pm}$ and $\epsilon_0^{\pm}$ on both filaments. The actual binding and unbinding rates are thus written as

$$\pi_{\pm} = \pi_0^{\pm}(1 - n_{\pm}), \quad \epsilon_{\pm} = \epsilon_0^{\pm} n_{\pm} \exp(F_{\pm}/f_c). \tag{33}$$

This bias in rates causes motors on one side of the model axoneme to detach faster than on the other side, resulting in asymmetric bending. The new characteristic motor correlation timescale is now defined as $\tau_0 = 1/[\langle \pi_0 \rangle + \langle \epsilon_0 \rangle]$, which involves the mean binding and unbinding rates:

$$\langle \pi_0 \rangle = \frac{\pi_0^+ + \pi_0^-}{2}, \quad \langle \epsilon_0 \rangle = \frac{\epsilon_0^+ + \epsilon_0^-}{2}. \tag{34}$$

Simulating cilialike beating patterns requires adjusting parameter values. Cilia come in a variety of lengths in the range of $L \sim 4\text{–}20\,\mu\text{m}$ [15] but are typically shorter than human sperm flagella. We choose a bending rigidity of $B \sim 5 \times 10^{-23}\,\text{N}\,\text{m}^2$, which is slightly larger than that reported in Ref. [44]. The characteristic time scale $\tau_0 \approx 40\,\text{ms}$ is chosen to produce a dimensional beating frequency of $f \sim 10\text{–}20\,\text{Hz}$, which is typical of mucociliary transport [47]. With a choice of $L \approx 8\,\mu\text{m}$, we estimate the typical sperm number to be $\text{Sp} \sim 2\text{–}3$. A typical waveform produced with these parameter is shown in Fig. 6(b), and is characterized by distinct power and recovery strokes with curvature variations that propagate from base to tip. The shown waveform, which captures the salient features of ciliary beats, oscillates at a frequency of $f \approx 13\,\text{Hz}$.

2. Breaststroke patterns: Curvature control

As they perform their breaststroke, the two flagella of *Chlamydomonas* also undergo asymmetric patterns, with distinctly different waveforms from those of cilia. There have been fewer attempts in simulating these patterns. A modified version of the geometric-clutch mechanism was used in Ref. [48] that involved force-velocity relationships allowing for asymmetric flagellar beats similar to *Chlamydomonas*. Further developments of the geometric-clutch model [20] with excitable dynein kinetics were able to reproduce breaststrokelike beating patterns. Recently, Sartori *et al.* [18] analyzed the axonemes of both *wild-type* and *mbo2* strains of *Chlamydomonas*. Through Fourier decomposition of waveforms and a numerical fitting procedure, they found that sliding control provides a poor fit for the waveform. Instead, curvature-control mechanisms provide the best fit to experimental data. Quite surprisingly, they noted that it is the rate of change of curvature that most likely controls the dynein activity. They also reported that the flagella have a nonzero static mode, suggesting an intrinsic curvature. However, their model neglected spatial variations of the motor control mechanism by nonuniform dynein distributions.

Our approach to capturing the beating patterns of *Chlamydomonas* is qualitative and extends the model discussed above for cilia. In addition to biased kinetics, we now also incorporate spontaneous filament curvature as well as a direct feedback from curvature on the dynein kinetics, whose detachment rate we model as

$$\epsilon_{\pm} = \epsilon_0^{\pm} n_{\pm} \exp\left(F_{\pm}/f_c \pm \kappa/\kappa_c\right), \tag{35}$$

where $\kappa(s, t)$ is the local curvature and κ_c is the critical value beyond which motors start to unbind. We set a constant nonzero intrinsic curvature $\kappa_0 = \phi_s^0$ that allows the flagella to spontaneously bend in absence of dynamic forces from the motors. With these modifications, the sliding displacement is now calculated from this reference configuration as $\Delta(s, t) = \phi(s, t) - \phi^0(s) = \phi(s, t) - \kappa_0 s$.

A typical waveform obtained with this model is shown in Fig. 6(c) and resembles that of a wild-type *Chlamydomonas* flagellum. Parameters for this case were estimated as follows. *Chlamydomonas reinhardtii* has a typical body size of $7\text{–}10\,\mu\text{m}$ with two flagella of length $10\text{–}12\,\mu\text{m}$ [49]. The bending rigidity of the axoneme is estimated to be $B \sim 5.8 \times 10^{-22}\,\text{N}\,\text{m}^2$. With these values,
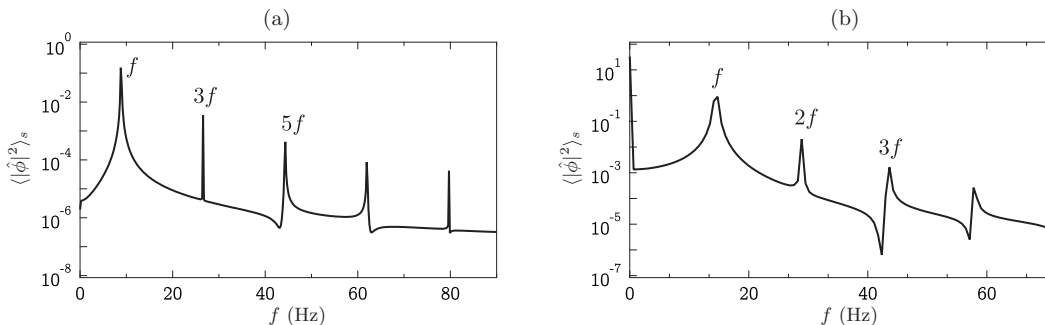
FIG. 7. Power spectral density $\langle |\hat{\phi}|^2 \rangle_s$ of the averaged tangent angle for: (a) a spermlike symmetric waveform and (b) *Chlamydomonas*-like breaststroke. Parameters are the same as in Figs. 6(a) and 6(c).

our numerical experiments indicate that waveforms of the type shown in Fig. 6(c) are possible for Sp $\sim$ 2–3. Using a characteristic time scale of $\tau_0 \approx 40$ ms, we observe a beating frequency $f \sim$ 12–15 Hz, which is lower than the typical frequency of 50–60 Hz observed in experiments.

IV. WAVEFORM ANALYSIS

A. Tangent angle dynamics and motor populations

We provide more quantitative details on the various waveforms of Fig. 6 by analyzing tangent angle and motor population dynamics. Following Sartori *et al.* [50], we first present results on the power spectrum of the mean tangent angle, which is defined as $\langle \phi(t) \rangle_s = \int_0^L \phi(s,t)\,ds$. We show its power spectral density $\langle |\hat{\phi}|^2 \rangle_s$ for spermlike and *Chlamydomonas*-like beats in Fig. 7, where we observe distinct peaks at the various harmonics of the fundamental frequency f. In the case of symmetric spermlike beats, only odd harmonics appear in the spectrum, which is a direct consequence of the symmetry property $\phi(s, t + T/2) = -\phi(s,t)$, where $T = 1/f$ is the period of oscillation. The *Chlamydomonas* waveform exhibits both odd and even harmonics, including a peak at zero frequency that points to the static mode of deformation $\phi^0(s)$ induced by the imposed spontaneous curvature. The spectrum produced by our model is qualitatively very similar to that measured in wildtype *Chlamydomonas reinhardtii* [18].

More details on the tangent angle and motor population dynamics are provided in Fig. 8, where we plot ϕ and $n_\pm$ at the filament midpoint ($s = 1/2$) as functions of time for the three beating patterns of Fig. 6. These quantities were previously reported by Oriola *et al.* [5] close to the initial Hopf bifurcation, where the tangent angle and bound motor distributions were found to have similar waveforms with a constant phase difference. In the nonlinear regime, these waveforms start to differ as highlighted in Fig. 8. The case of spermlike beats in Fig. 8(a) is characterized by a symmetric waveform for ϕ, which shares striking similarities with the experimental measurements of Riedel-Kruse *et al.* [6]. The two antagonistic motor populations have identical phase-shifted evolutions, which is expected for symmetric beats. They also show cusp-shaped oscillations that are characteristic of far-from-equilibrium dynamics [25,41]. Quite remarkably, we find that only a fairly small fraction of bound dyneins is required to produce oscillations [5]. Figures 8(b) and 8(c) show the dynamics for ciliary and breaststroke patterns, respectively, and look qualitatively different from the case of sperm. In particular, the tangent angle evolution shows sharp cusps, with distinct rates of growth and decay that are indicative of the asymmetric power and recovery strokes. The cusps in the dynamics of ϕ are accompanied by abrupt changes in the bound dynein populations, with n_+ and n_- now showing distinct waveforms as a result of biased kinetics. It is useful to recall that the kinetics of dynein motors in our model does not account for any form of motor transport along the arc-length, and as a result sharp changes in bound motor fractions are permissible when the local
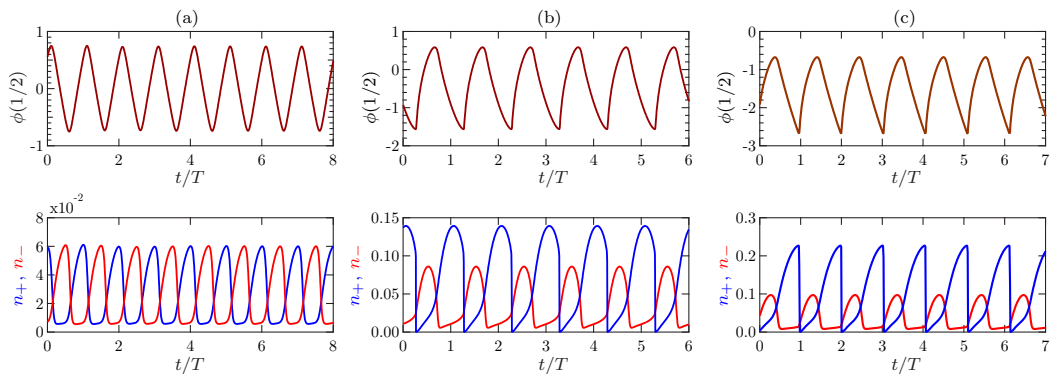
FIG. 8. Tangent angle and motor population dynamics in the case of (a) spermlike, (b) cilialike, and (c) *Chlamydomonas*-like beating patterns. The top panel shows the evolution of the tangent angle $\phi(s,t)$ measured at the midpoint of the filament ($s = 1/2$). The bottom panel shows the evolution of corresponding bound motor populations $n_+(s,t)$ and $n_-(s,t)$, also evaluated at the midpoint. Parameters are the same as described in the caption of Fig. 6.

rate of attachment changes sign. It is likely that some amount of diffusion is present in biological systems and would somewhat smoothen motor population dynamics [51].

B. Reduced-order dynamics and limit cycles

The set of partial differential equations governing the evolution of the tangent angle $\phi(s,t)$ can be interpreted as an infinite dimensional dynamical system. As previously discussed, this dynamical system undergoes a Hopf bifurcation with increasing activity, leading to limit-cycle oscillations. In the standard analysis of Hopf bifurcations [52], limit cycles are typically described in terms of a characteristic radius r and a phase χ that grows linearly with time. This suggests seeking a lower-dimensional approximation of the full dynamical system that coarse-grains the dynamics into a simpler oscillator while retaining its essential features. Several studies of hydrodynamic synchronization have proposed similar approaches [53–55]. Here, we apply tools from principal component analysis (PCA) to describe the waveforms, as was previously done in the past to analyze flagellar beats [5,27,56]. We restrict our analysis to sperm and ciliary beating patterns, as the breaststroke waveforms reveal very similar results as cilia.

A spatiotemporal representation of the beating patterns is first obtained in Figs. 9(a) and 9(d) where we plot the tangent angle $\phi(s,t)$ as a function of both s and t. These so-called "kymographs" are qualitatively similar to those obtained experimentally for both sperm and cilia, and clearly highlight the periodic nature of the dynamics, with bending waves that propagate from base ($s = 0$) to tip ($s = 1$). To further characterize deformations, we first define the covariance function $C(s,s')$ as

$$C(s,s') = \int_0^T \int_0^T [\phi(s,t) - \langle\phi(s,t)\rangle_t][\phi(s',t') - \langle\phi(s',t')\rangle_{t'}]\, dt\, dt', \tag{36}$$

where $\langle\phi(s,t)\rangle_t = \frac{1}{T}\int_0^T \phi(s,t)dt$ is the time average of the tangent angle over one period and $C(s,s')$ is symmetric with respect to s and s' by construction. It is depicted in Figs. 9(b) and 9(e) for both sperm and cilia waveforms. In both cases, strong correlations are observed near the main diagonal, which are indicative of the finite bending stiffness [5,27]. In the case of spermlike beats in Fig. 9(b), negatively correlated regions appear at a distance of $s = \lambda/2$ away from the diagonal, which is characteristic of propagating bending waves and provides another estimate of the wavelength. The number of local maxima in Fig. 9(b) is accounted by the wavenumber of the
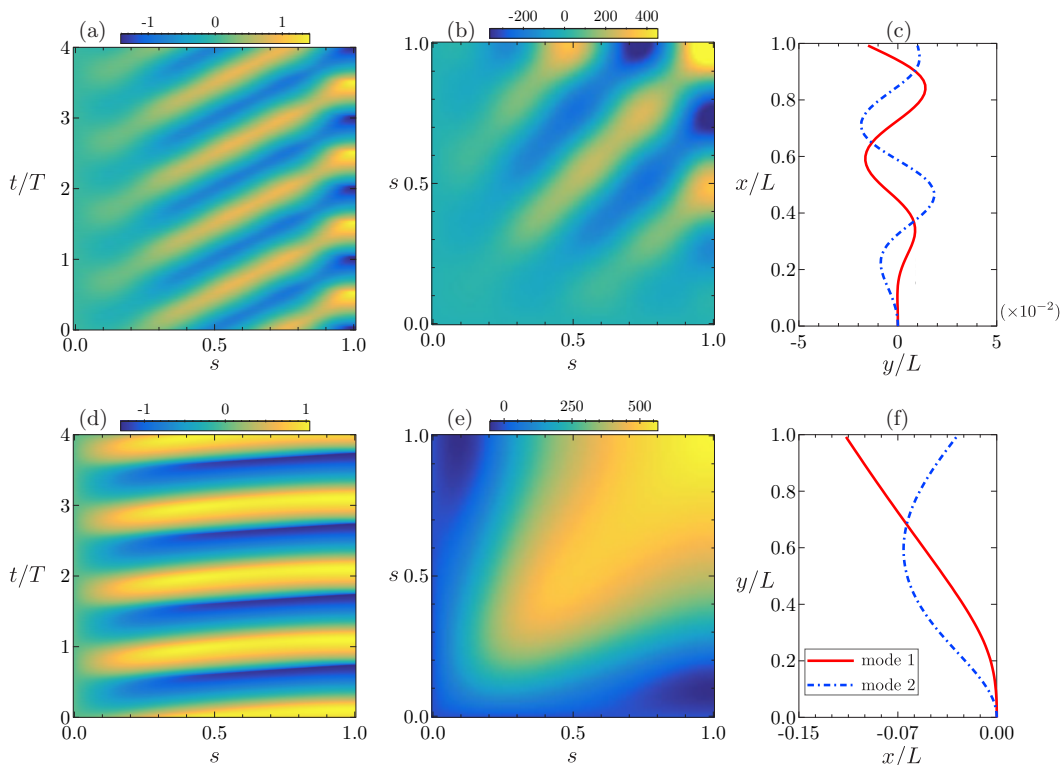
FIG. 9. The first row shows: (a) the kymograph, (b) the covariance function C, and (c) the two dominant mode shapes from PCA in the case of a symmetric spermlike beat. The bottom row (d, e, f) shows the same for the ciliary beating pattern. Parameters are identical to Figs. 6(a) and 6(b).

traveling waves [5]. Close to the Hopf bifurcation, the number of local maxima decreases with increasing activity; however, as discussed previously in Fig. 5, this behavior is not necessarily true in the nonlinear regime where abrupt transitions in wavenumbers can occur. Interestingly, we do not observe any negative correlations in the case of ciliary waveforms in Fig. 9(e), where the covariance instead systematically decays away from the diagonal.

To obtain a reduced-order representation of the dynamics, we apply PCA, which relies on the spectral decomposition of the covariance in terms of orthogonal deformation eigenmodes $\psi_n(s)$ with corresponding eigenvalues σ_n:

$$C(s, s') = \sum_{n=1}^{\infty} \sigma_n \psi_n(s) \psi_n(s'). \tag{37}$$

These modes are determined numerically by discretizing arclength into $M - 1$ segments and evaluating the covariance by quadrature. This produces a $M \times M$ symmetric positive matrix $C(s_i, s_j)$, which admits real positive eigenvalues $\sigma_1 \geqslant \sigma_2 \geqslant \dots \geqslant \sigma_M > 0$ and real orthogonal eigenvectors describing fundamental modes of deformation. The first few eigenmodes are expected to capture the dominant spatial features of the waveforms, and in all the beat patterns considered here we find that truncating Eq. (37) after two terms provides a good approximation with less than 4 % error [27]. Waveforms at any instant can now be approximated as a linear combination of eigenmodes. In the spirit of dimensional reduction [57], we propose an approximate representation in terms of the
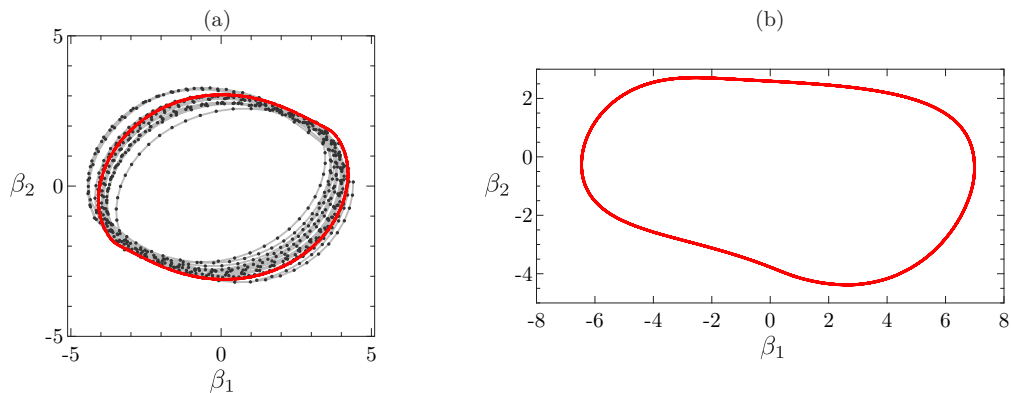
FIG. 10. Limit cycle representation for (a) spermlike and (b) ciliary beating patterns. The red curves show the deterministic limit cycles. In panel (a), the gray points show deviations from the deterministic cycle due to biochemical noise.

two dominant modes:

$$\phi(s,t) \approx \phi^0(s) + \beta_1(t)\psi_1(s) + \beta_2(t)\psi_2(s), \tag{38}$$

where $\phi^0(s)$ is the mean filament shape. The two coefficients $\{\beta_1, \beta_2\}$, known as "shape scores" [27], capture the temporal evolution of the fundamental modes and can be calculated numerically by least-squares minimization. The two dominant PCA modes $\psi_1(s)$ and $\psi_2(s)$ are depicted in Figs. 9(c) and 9(f) for sperm and ciliary beats.

Within the approximation of Eq. (38), the temporal dynamics of a beating filament is represented as a trajectory in the two-dimensional phase space of $\{\beta_1, \beta_2\}$, where periodic waveforms are described by limit cycles. Figure 10(a) shows the reconstructed limit cycle for the symmetric spermlike beat, both in the absence and presence of biochemical noise. In the absence of noise, the limit cycle has a characteristic shape with axial symmetry, which is more regular than that previously obtained close to the bifurcation limit [5]. Expectedly, biochemical noise leads to deviations from this periodic trajectory, with the system randomly exploring a band of possible states surrounding the deterministic cycle, as also seen in experimental waveforms [27,56]. The deviations from the deterministic cycle are found to be nonuniform along the cycle, suggesting that certain filament conformations are more susceptible to noise than others; this curious feature is also observed experimentally [56]. The limit cycle for the cilialike waveform is shown in Fig. 10(b) and is strikingly different, with an elongated asymmetric shape resulting from the asymmetry of the beating pattern.

V. FLOW FIELDS AND FUNDAMENTAL SINGULARITIES

A. Instantaneous and time-averaged flow fields

We now proceed to analyze the flow fields generated by the beating filaments and their descriptions in terms of fundamental singularities of Stokes flow. In the Stokes regime, the velocity at any point $\mathbf{x}$ in the fluid is simply obtained in terms of the force distribution along the filament. In dimensionless form, it reads

$$\mathbf{u}(\mathbf{x},t) = \frac{1}{\mathrm{Sp}^4} \int_0^1 \mathbf{G}(\mathbf{x}, \mathbf{x}_0) \cdot \mathbf{f}_e(s_0, t)\, ds_0, \tag{39}$$

where $\mathbf{x}_0 = \mathbf{x}(s_0, t)$ is the Lagrangian point parametrized by arclength s_0 along the filament, $\mathbf{f}_e(s_0, t)$ is the local force per unit length exerted by the filament on the fluid, and $\mathbf{G}(\mathbf{x}, \mathbf{x}_0)$ is the appropriate

Green's function scaled by $1/(8\pi\nu L)$. In free space, **G** is simply given by the Oseen tensor. We also consider the case of a filament clamped against a flat wall, for which we use Blake's solution [35] for a point force next to a no-slip boundary. Note that the description of the disturbance flow field in terms of point forces in Eq. (39) becomes inaccurate very close to the filaments, where it can be improved using a distribution of source doublets [31] that scale as ϵ^2/r^3, where r is distance from the filament and ϵ is the aspect ratio. This correction, however, only modifies the flow in the close vicinity of the filaments and does not alter the large-scale features of the disturbance fields.

Snapshots of instantaneous flows fields at three instants over the course of one beating period are shown in Fig. 11, where we consider both sperm and ciliary beats in free space, as well as a cilium next to a no-slip wall. As expected, velocities are largest close to the filament, with maximum values attained near the inflection points of the waveform in the case of sperm, and near the tip of the filament in the case of cilia. In free space, the flow field away from the filament resembles the well-known Stokeslet flow field, which decays as $1/r$ in three dimensions. This does not come as a surprise as the filaments are not force-free in our model: in an experiment on spermatozoa, the net force imparted by the flagellum would instead balance the drag on the sperm head, resulting a net dipolar flow decaying as $1/r^2$. The case of a cilium next to a no-slip wall is shown in Fig. 11(c) and exhibits a qualitatively different flow field, with the appearance of recirculation regions for certain conformations [58]. In this case, the Stokeslet contribution induced by the filament is canceled by the presence of the wall, resulting in a net flow that is either dipolar or quadrupolar, depending on the orientation of the applied force [35]: for a point force oriented parallel to the wall, the flow field is dipolar with a characteristic $1/r^2$ decay, while it is quadrupolar for a point force oriented perpendicular to the wall with a far-field decay of $1/r^3$.

These observations are substantiated in Fig. 12, showing the time-averaged velocity fields for the same beating patterns, as well as the spatial decay of the velocity magnitude. Both cases in free space resemble Stokeslet flows and indeed exhibit a far-field decay of $1/r$. In the case of the ciliary beat above a no-slip boundary, the flow has a more complex structure with a recirculation bubble next to the wall, and also shows a much slower decay of $1/r^3$, which suggests that on average the net force exerted by the filament is normal to the wall [53].

Another interesting aspect revealed by the average flow fields is the net direction of pumping. In the case of a clamped sperm with anterograde wave propagation as shown in Fig. 12(a), flagellar oscillations drive a net flow from tip to tail, which, in the case of a force-free cell, would enable propulsion in the forward direction. However, simulations at lower activity levels (not shown) reveal that the direction of propulsion is reversed when waves propagate in the retrograde direction. This hints at the importance of dynein level regulation for efficient sperm motility, and also has consequences for the hydrodynamic synchronization of nearby interacting flagella [59].

B. Singularity representation

The linearity of the Stokes equations allows us to represent the flow fields in terms of fundamental singular solutions. Several methods have been proposed for seeking such representations. In a simple model, Brumley *et al.* [55] used a single time-dependent Stokeslet to approximate the flow field of a *Volvox carteri* colony held in place by a micropipette. A more general method consists of seeking an unsteady multipole expansion [60], which was applied to describe the flow field generated by swimming *Chlamydomonas* [61]. More recently, PCA was also used to identify dominant contributions to the velocity fields. These modes were then approximated by a set of regularized Stokeslets [58] for quantitative representations of the flow fields [62,63]. Here, we adopt this approach and apply it to analyze the flow field generated by a clamped sperm.

The numerical determination of the PCA modes involves similar steps as discussed in Sec. IV B for the analysis of waveforms and proceeds as follows. We focus on two-dimensional flow fields in the plane of motion, and first compute q snapshots of the velocity field on a $N \times N$ Cartesian grid over the course of one period of oscillation. In contrast to past studies [62], we do not subtract the time-averaged velocity field as usually done in PCA; this does not affect the representation of the
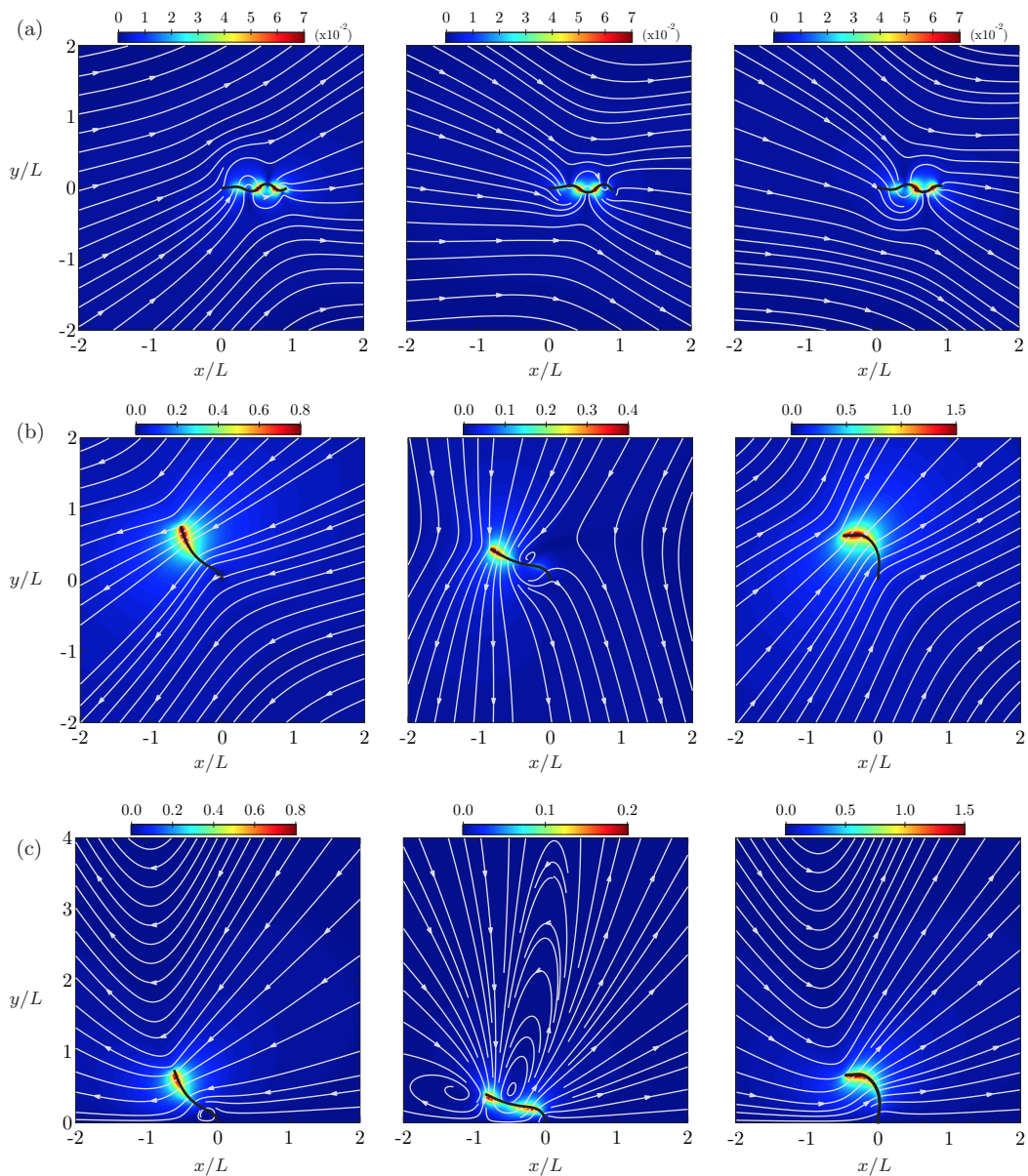
FIG. 11. Magnitude and streamlines of the instantaneous velocity field obtained using Eq. (39) for three representative cases: (a) spermlike beating pattern in free space, (b) ciliary beat in free space, and (c) ciliary beat against a no-slip wall at $y = 0$. The three columns correspond to three time instants during one period of oscillation. Also see the movies of the instantaneous flow fields in the Supplemental Material [42].

flow field due to the linearity of Stokes flow. Each such snapshot contains $2N^2$ values for the two velocity components (u_x, u_y), which are used to populate the rows of a matrix $M \in \mathbb{R}^{q \times 2N^2}$:

$$\mathbf{v}_\alpha = \text{row}_\alpha M = \left[u_x^1, u_x^2, \cdots u_x^{N^2}, u_y^1, u_y^2, \cdots u_y^{N^2} \right]_\alpha, \quad \text{for } \alpha = 1, 2, ..., q. \tag{40}$$
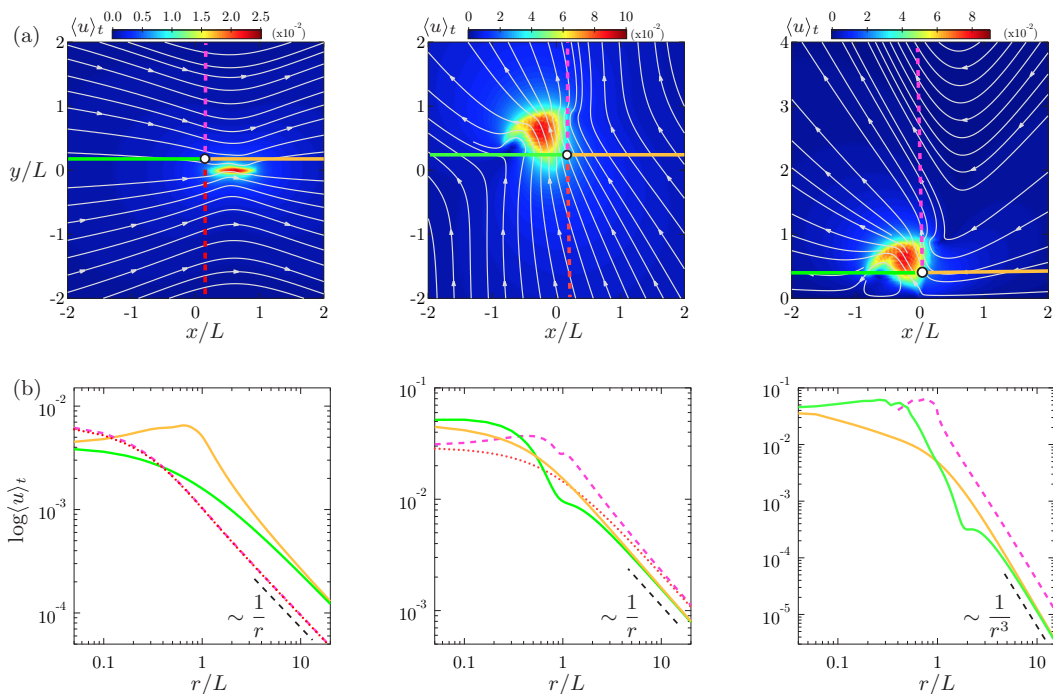
FIG. 12. (a) Streamlines and magnitude of the time-averaged velocity field $\langle \mathbf{u} \rangle_t$ for the three cases shown in Fig. 11. From left to right: sperm in free space, cilium in free space, and cilium against a no-slip wall. (b) Log-log plot of the time-averaged velocity magnitude vs. distance. The colors are associated with the lines along which the velocity are evaluated as shown in panel (a). In free space, the velocity fields show a decay of $1/r$ characteristic of a net Stokeslet. In the case of a cilium next to a wall, a faster decay of $1/r^3$ is found, which corresponds to a net force perpendicular to the no-slip wall.

We then define the $2N^2 \times 2N^2$ covariance matrix $C = M^T M$, which encapsulates spatial features of the velocity field irrespective of time. The matrix C is real symmetric positive definite and thus admits an eigendecomposition in terms of real orthogonal basis vectors $\mathbf{V}^{(i)}(\mathbf{x}) \in \mathbb{R}^{2N^2}$, where, $i = 1, ..., 2N^2$. For all the beating patterns presented here, we find that the first 3 to 5 eigenmodes are sufficient to capture 95 % of the cumulative variations in the data. In the case of sperm, an excellent representation of the velocity field can be achieved as a linear combination of the three dominant modes:

$$\mathbf{u}^d(\mathbf{x}, t) = \alpha_1(t)\mathbf{V}^{(1)}(\mathbf{x}) + \alpha_2(t)\mathbf{V}^{(2)}(\mathbf{x}) + \alpha_3(t)\mathbf{V}^{(3)}(\mathbf{x}), \tag{41}$$

where the time-dependent coefficients are determined by least-squares minimization. The first three PCA modes $\mathbf{V}^{(i)}(\mathbf{x})$ are illustrated in Fig. 13, and the corresponding amplitudes $\alpha_i(t)$ are show in Fig. 14(a). The dominant mode ($i = 1$), which is almost steady, resembles the flow due to a Stokeslet and captures the net streaming motion induced by the filament. The next two modes ($i = 2, 3$) have a more complex spatial structure with multiple velocity peaks that echo the structure of the deformation eigenmodes found in Fig. 9(c). These two modes are oscillatory with a constant phase difference and account for unsteady flow dynamics resulting from filament deformations.

These various PCA modes can be further approximated in terms of collections of regularized Stokeslets [58,64]. The flow field generated by a single regularized Stokeslet with regularization
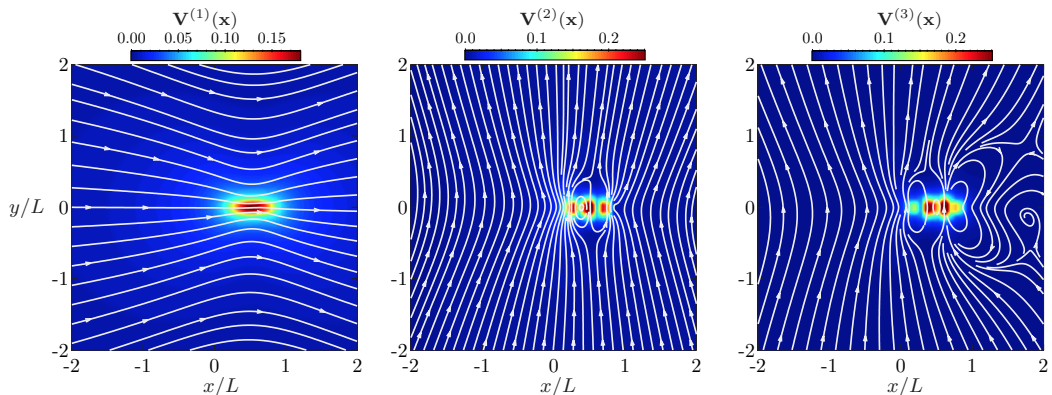
FIG. 13. First three PCA velocity modes $\mathbf{V}^{(i)}(\mathbf{x})$ ($i = 1, 2, 3$) for a clamped beating sperm. The first mode is dominated by a Stokeslet flow, whereas the next two modes have a more complex spatial structure with multiple velocity peaks that echo the structure of the deformation eigenmodes found in Fig. 9(c). All three velocity fields can be approximated in terms of regularized Stokeslets.

parameter ε and strength $\mathbf{f}$ is given by

$$\mathbf{u}^S(\mathbf{x}; \varepsilon) = \left[\frac{(r^2 + 2\varepsilon^2)\mathbf{I} + \mathbf{rr}}{(r^2 + \varepsilon^2)^{3/2}} \right] \cdot \mathbf{f}, \tag{42}$$

where $\mathbf{r} = \mathbf{x} - \mathbf{x}_0$ and $\mathbf{x}_0$ is the location of the singularity. Following Ishimoto *et al.* [62], we represent each mode in terms of p Stokeslets, where the parameters $(\varepsilon^p, x_0^p, y_0^p, f_x^p, f_y^p)$ are calculated through a least-squares solution that implements a Levenberg-Marquardt algorithm. The number p is chosen such that we obtain a satisfactory approximation to the basis vectors, and in the present case we use $p = 2$, 5, and 6 for each for the first three modes. A typical flow field obtained by this reconstruction method is compared to the full numerical flow field in Figs. 14(b) and 14(c), where excellent agreement is found.
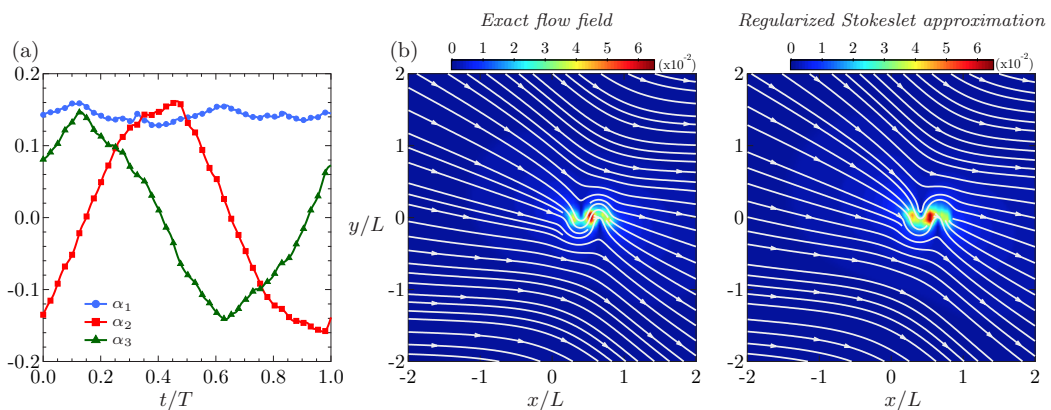

FIG. 14. (a) Variation of the weighting coefficients $\alpha_i(t)$ of the three PCA velocity modes shown in Fig. 13 over one period of oscillation. (b) Comparison of the approximated instantaneous flow-field (right) to the exact numerical one (left) at $t/T = 0.9$.

VI. CONCLUSION

In this paper, we have used numerical simulations of a sliding control model of the axoneme to highlight how spontaneous oscillations can emerge from the collective action of molecular motors. Our model for coupled elastohydrodynamics and motor kinetics follows that previously proposed by Oriola *et al.* [5] and allows for saturation of unstable modes following a Hopf bifurcation that leads to the propagation of bending waves resembling the beating patterns of spermatozoa. While the study of Oriola *et al.* [5] as well as other related numerical models [6,23,41] were restricted to the small curvature limit where retrograde wave propagation takes place, our fully nonlinear simulations demonstrated the existence of a second transition at higher activity levels giving rise to anterograde wave propagation consistent with observations of sperm [38]. Unlike previous studies that used local resistive force theory to capture viscous stresses, our model also accounts for nonlocal hydrodynamic interactions based on slender-body theory, and these interactions are found to change the instability threshold quantitatively even though the qualitative behavior remains unchanged. We also demonstrated the ability of our model to capture asymmetric beating patterns resembling those of cilia and of *Chlamydomonas* flagella, which were obtained using a combination of biased motor kinetics and curvature control. While quantitative comparison of the obtained waveforms with experimental data [18] remains a challenge, the qualitative agreement is promising. Tools from principle component analysis were also applied for dimensional reduction and allowed us to describe the beating patterns in terms of simplified limit-cycle dynamics reminiscent of a canonical Hopf oscillator. We also explored the role of biochemical noise, which causes deviations from these limit cycles in qualitative agreement with experimental measurements [27].

Our model also allowed us to analyze disturbance flows induced by beating filaments, which are known in biological systems to play a crucial role in development, motility, and sensing. It has been a long-standing hypothesis that these flow fields may be responsible for flagellar synchronization. The phase synchronization of nearby swimming sperm and the synchronous beating of biflagellated *Chlamydomonas* algae have indeed been observed experimentally [65], and the cilia lining the surface of squirming cells such as *Paramecium* are also well known to exhibit coordinated beats in the form of metachronal waves. A number of theoretical and computational models [14,41,43,45,66,67] have been applied to elucidate mechanisms for synchronization and metachronal wave formation, yet most of them either rely on an internal driving engine to generate beats or completely coarse-grain motor activity. While these approaches provide interesting insight, they miss crucial aspects of internal axonemal mechanics and their coupling to motor kinetics. The mathematical model and numerical tools developed here provide a foundation for addressing these questions in a more realistic framework, where we can also account for the role of biochemical noise in driving the "phase slips" observed in biological systems [65].

There remains a number of avenues in which the presented model could be improved or extended. We have entirely focused on clamped boundary conditions, while it may be also interesting to consider pivoting boundary conditions and include provisions for basal sliding. Since our model is based on a two-dimensional projection of the three-dimensional axoneme, emergent beating patterns are planar only. Including a more realistic representation of the 3D axonemal structure is challenging but would allow for twist, which is known to lead to different beating patterns [50]. Recently, Pearce *et al.* [51] proposed a formulation with curvature-sensitive kinesin binding dynamics to explain ring formations in gliding microtubule assays. Their model also shows potential for ciliary beating patterns and can be included in the present framework to improve the basic curvature-control model.

---

[1] B. Alberts, D. Bray, K. Hopkin, A. Johnson, J. Lewis, M. Raff, K. Roberts, and P. Walter, *Essential Cell Biology* (Garland Science, New York, 2013).

[2] M. A. Sleigh, J. R. Blake, and N. Liron, The propulsion of mucus by cilia, Am. Rev. Respir. Dis. **137**, 726 (1988).

[3] E. F. Smith and P. A. Lefebvre, PF16 encodes a protein with armadillo repeats and localizes to a single microtubule of the central apparatus in *Chlamydomonas* flagella, J. Cell biol. **132**, 359 (1996).

[4] C. D. Silflow and P. A. Lefebvre, Assembly and motility of eukaryotic cilia and flagella. lessons from *Chlamydomonas reinhardtii*, Plant Physiol. **127**, 1500 (2001).

[5] D. Oriola, H. Gadêlha, and J. Casademunt, Nonlinear amplitude dynamics in flagellar beating, R. Soc. Open Sci. **4**, 160698 (2017).

[6] I. H. Riedel-Kruse, A. Hilfinger, J. Howard, and F. Jülicher, How molecular motors shape the flagellar beat, HFSP J. **1**, 192 (2007).

[7] K. E. Summers and I. R. Gibbons, Adenosine triphosphate-induced sliding of tubules in trypsin-treated flagella of sea-urchin sperm, Proc. Natl. Acad. Sci. USA **68**, 3092 (1971).

[8] S. Camalet and F. Jülicher, Generic aspects of axonemal beating, New J. Phys. **2**, 24 (2000).

[9] P. V. Bayly and S. K. Dutcher, Steady dynein forces induce flutter instability and propagating waves in mathematical models of flagella, J. R. Soc. Interface **13**, 20160523 (2016).

[10] G. De Canio, E. Lauga, and R. E. Goldstein, Spontaneous oscillations of elastic filaments induced by molecular motors, J. R. Soc. Interface **14**, 20170491 (2017).

[11] F. Ling, H. Guo, and E. Kanso, Instability-driven oscillations of elastic microfilaments, J. R. Soc. Interface **15**, 20180594 (2018).

[12] V. V. Bolotin, *Nonconservative Problems of the Theory of Elastic Stability* (Macmillan, London, 1963).

[13] R. Chelakkot, A. Gopinath, L. Mahadevan, and M. F. Hagan, Flagellar dynamics of a connected chain of active, polar, Brownian particles, J. R. Soc. Interface **11**, 20130884 (2014).

[14] R. E. Goldstein, E. Lauga, A. I. Pesci, and M. R. E. Proctor, Elastohydrodynamic synchronization of adjacent beating flagella, Phys. Rev. Fluids **1**, 073201 (2016).

[15] R. H. Dillon and L. J. Fauci, An integrative model of internal axoneme mechanics and external fluid dynamics in ciliary beating, J. Theor. Biol. **207**, 415 (2000).

[16] C. J. Brokaw, Bend propagation by a sliding filament model for flagella, J. Exp. Biol. **55**, 289 (1971).

[17] M. Hines and J. J. Blum, Bend propagation in flagella. I. Derivation of equations of motion and their simulation, Biophys. J. **23**, 41 (1978).

[18] P. Sartori, V. F. Geyer, A. Scholich, F. Jülicher, and J. Howard, Dynamic curvature regulation accounts for the symmetric and asymmetric beats of *Chlamydomonas* flagella, Elife **5**, e13258 (2016).

[19] C. B. Lindemann, A "geometric clutch" hypothesis to explain oscillations of the axoneme of cilia and flagella, J. Theor. Biol. **168**, 175 (1994).

[20] P. V. Bayly and K. S. Wilson, Equations of interdoublet separation during flagella motion reveal mechanisms of wave propagation and instability, Biophys. J. **107**, 1756 (2014).

[21] P. V. Bayly and K. S. Wilson, Analysis of unstable modes distinguishes mathematical models of flagellar motion, J. R. Soc. Interface **12**, 20150124 (2015).

[22] H. Gadêlha, E. A. Gaffney, D. J. Smith, and J. C. Kirkman-Brown, Nonlinear instability in flagellar dynamics: A novel modulation mechanism in sperm migration? J. R. Soc. Interface **7**, 1689 (2010).

[23] A. Hilfinger, A. K. Chattopadhyay, and F. Jülicher, Nonlinear dynamics of cilia and flagella, Phys. Rev. E **79**, 051918 (2009).

[24] S. Camalet, F. Jülicher, and J. Prost, Self-Organized Beating and Swimming of Internally Driven Filaments, Phys. Rev. Lett. **82**, 1590 (1999).

[25] F. Jülicher and J. Prost, Spontaneous Oscillations of Collective Molecular Motors, Phys. Rev. Lett. **78**, 4510 (1997).

[26] B. Guirao and J.-F. Joanny, Spontaneous creation of macroscopic flow and metachronal waves in an array of cilia, Biophys. J. **92**, 1900 (2007).

[27] S. Werner, J. C. Rink, I. H. Riedel-Kruse, and B. M. Friedrich, Shape mode analysis exposes movement patterns in biology: Flagella and flatworms as case studies, PloS One **9**, e113083 (2014).

[28] S. S. Antman, *Nonlinear Problems of Elasticity* (Springer, New York, 1995).

[29] J. Keller and S. Rubinow, Slender-body theory for slow viscous flow, J. Fluid Mech. **75**, 705 (1976).

[30] R. E. Johnson, An improved slender-body theory for Stokes flow, J. Fluid Mech. **99**, 411 (1980).

[31] A.-K. Tornberg and M. J. Shelley, Simulating the dynamics and interactions of flexible fibers in Stokes flows, J. Comput. Phys. **196**, 8 (2004).

[32] L. Koens and E. Lauga, The boundary integral formulation of Stokes flow includes slender-body theory, J. Fluid Mech. **850**, R1 (2018).

[33] J. Gray and G. J. Hancock, The propulsion of sea-urchin spermatozoa, J. Exp. Biol. **32**, 802 (1955).

[34] J. Lighthill, Flagellar hydrodynamics, SIAM Rev. **18**, 161 (1976).

[35] J. R. Blake, A note on the image system for a stokeslet in a no-slip boundary, Math. Proc. Cambridge Phil. Soc. **70**, 303 (1971).

[36] K. Svoboda and S. M. Block, Force and velocity measured for single kinesin molecules, Cell **77**, 773 (1994).

[37] M. J. I. Müller, S. Klumpp, and R. Lipowsky, Tug-of-war as a cooperative mechanism for bidirectional cargo transport by molecular motors, Proc. Natl. Acad. Sci. USA **105**, 4609 (2008).

[38] E. A. Gaffney, H. Gadêlha, D. J. Smith, J. R. Blake, and J. C. Kirkman-Brown, Mammalian sperm motility: Observation and theory, Annu. Rev. Fluid Mech. **43**, 501 (2011).

[39] J. Howard, *Mechanics of Motor Proteins and the Cytoskeleton* (Sinauer Associates, Sunderland, MA, 2001).

[40] D. J. Smith, E. A. Gaffney, H. Gadêlha, N. Kapur, and J. C. Kirkman-Brown, Bend propagation in the flagella of migrating human sperm, and its modulation by viscosity, Cytoskeleton **66**, 220 (2009).

[41] T. Guérin, J. Prost, and J.-F. Joanny, Dynamical behavior of molecular motor assemblies in the rigid and crossbridge models, Eur. Phys. J. E **34**, 60 (2011).

[42] See Supplemental Material at http://link.aps.org/supplemental/10.1103/PhysRevFluids.4.043102 for various movies showing temporal dynamics.

[43] J. Elgeti and G. Gompper, Emergence of metachronal waves in cilia arrays, Proc. Natl. Acad. Sci. USA **110**, 4470 (2013).

[44] S. Gueron and N. Liron, Ciliary motion modeling, and dynamic multicilia interactions, Biophys. J. **63**, 1045 (1992).

[45] S. Gueron, K. Levit-Gurevich, N. Liron, and J. J. Blum, Cilia internal mechanism and metachronal coordination as the result of hydrodynamical coupling, Proc. Natl. Acad. Sci. USA **94**, 6001 (1997).

[46] J. Han and C. S. Peskin, Spontaneous oscillation and fluid–structure interaction of cilia, Proc. Natl. Acad. Sci. USA **115**, 4417 (2018).

[47] P. Delmotte and M. J. Sanderson, Ciliary beat frequency is maintained at a maximal rate in the small airways of mouse lung slices, Am. J. Respir. Cell Mol. Biol. **35**, 110 (2006).

[48] C. B. Lindemann, Geometric clutch model version 3: The role of the inner and outer arm dyneins in the ciliary beat, Cytoskeleton **52**, 242 (2002).

[49] J. S. Guasto, K. A. Johnson, and J. P. Gollub, Oscillatory Flows Induced by Microorganisms Swimming in Two Dimensions, Phys. Rev. Lett. **105**, 168102 (2010).

[50] P. Sartori, V. F. Geyer, J. Howard, and F. Jülicher, Curvature regulation of the ciliary beat through axonemal twist, Phys. Rev. E **94**, 042426 (2016).

[51] S. P. Pearce, M. Heil, O. E. Jensen, G. W. Jones, and A. Prokop, Curvature-sensitive kinesin binding can explain microtubule ring formation and reveals chaotic dynamics in a mathematical model, arXiv:1803.07312 (2018).

[52] S. H. Strogatz, *Nonlinear Dynamics and Chaos: With Applications to Physics, Biology, Chemistry, and Engineering* (CRC Press, Boca Raton, 2018).

[53] T. Niedermayer, B. Eckhardt, and P. Lenz, Synchronization, phase locking, and metachronal wave formation in ciliary chains, Chaos **18**, 037128 (2008).

[54] A. Vilfan and F. Jülicher, Hydrodynamic Flow Patterns and Synchronization of Beating Cilia, Phys. Rev. Lett. **96**, 058102 (2006).

[55] D. R. Brumley, K. Y. Wan, M. Polin, and R. E. Goldstein, Flagellar synchronization through direct hydrodynamic interactions, Elife **3**, e02750 (2014).

[56] R. Ma, G. S. Klindt, I. H. Riedel-Kruse, F. Jülicher, and B. M. Friedrich, Active Phase and Amplitude Fluctuations of Flagellar Beating, Phys. Rev. Lett. **113**, 048101 (2014).

[57] J. N. Kutz, *Data-Driven Modeling and Scientific Computation: Methods for Complex Systems and Big Data* (Oxford University Press, Oxford, 2013).

[58] J. Ainley, S. Durkin, R. Embid, P. Boindala, and R. Cortez, The method of images for regularized Stokeslets, J. Comput. Phys. **227**, 4600 (2008).

[59] B. Chakrabarti and D. Saintillan (unpublished).

[60] S. Ghose and R. Adhikari, Irreducible Representations of Oscillatory and Swirling Flows in Active Soft Matter, Phys. Rev. Lett. **112**, 118102 (2014).

[61] G. S. Klindt and B. M. Friedrich, Flagellar swimmers oscillate between pusher-and puller-type swimming, Phys. Rev. E **92**, 063019 (2015).

[62] K. Ishimoto, H. Gadêlha, E. A. Gaffney, D. J. Smith, and J. Kirkman-Brown, Coarse-Graining the Fluid Flow Around a Human Sperm, Phys. Rev. Lett. **118**, 124501 (2017).

[63] K. Ishimoto, H. Gadêlha, E. A. Gaffney, D. J. Smith, and J. Kirkman-Brown, Human sperm swimming in a high viscosity mucus analogue, J. Theor. Biol. **446**, 1 (2018).

[64] R. Cortez, The method of regularized Stokeslets, SIAM J. Sci. Comput. **23**, 1204 (2001).

[65] R. E. Goldstein, M. Polin, and I. Tuval, Noise and Synchronization in Pairs of Beating Eukaryotic Flagella, Phys. Rev. Lett. **103**, 168103 (2009).

[66] Y. Yang, J. Elgeti, and G. Gompper, Cooperation of sperm in two dimensions: Synchronization, attraction, and aggregation through hydrodynamic interactions, Phys. Rev. E **78**, 061903 (2008).

[67] S. F. Schoeller and E. E. Keaveny, From flagellar undulations to collective motion: Predicting the dynamics of sperm suspensions, J. R. Soc. Interface **15**, 20170834 (2018).